



# Diverging wave compounding with spatio-temporal encoding using orthogonal Golay pairs for high frame rate imaging

Feifei Zhao, Jianwen Luo\*

Department of Biomedical Engineering, School of Medicine, Tsinghua University, Beijing 100084, China

## ARTICLE INFO

### Keywords:

Diverging wave compounding  
Golay codes  
High frame rate  
Orthogonal

## ABSTRACT

Golay coded excitation for diverging wave compounding (DWC) has been demonstrated to increase the signal-to-noise ratio (SNR) and contrast for high frame rate cardiac imaging. However, the complementary codes need to be transmitted in two consecutive firings for decoding, which reduces the frame rate by 2 folds. This paper proposes an orthogonal Golay pairs coded (OGPs-coded) DWC sequence to overcome this problem, which implements spatio-temporal encoding for DWC. Two diverging waves (DWs) at different steering angles coded by an orthogonal Golay pair are transmitted *simultaneously*, thus compensating the frame rate reduction caused by transmissions of complementary codes. The two DWs can be separated based on the orthogonality of Golay pairs. To test the feasibility of the proposed sequence, we performed simulations of point targets and tissue phantoms in both static and moving states. Compared with non-coded DWC at the same frame rate, OGPs-coded DWC obtains comparable resolution, SNR gains of 7.5–10 dB and contrast gains of 3–5 dB. The OGPs-coded DWC sequence was also tested experimentally on a tissue-mimicking phantom. Compared with non-coded DWC, OGPs-coded DWC achieves improvements in the SNR (3–6 dB) and contrast (1–2 dB). Preliminary *in vivo* results show brighter myocardium and larger penetration depth with the proposed method. The proposed OGPs-coded DWC sequence has potential for high frame rate and high quality cardiac imaging.

## 1. Introduction

Ultrafast ultrasound imaging by transmitting unfocused waves has been proposed to dramatically reduce the number of transmits per image frame for ultrahigh frame rate. By transmitting only one unfocused wave, a relatively large imaging field-of-view and dense scan lines could be reconstructed from parallel beamforming. Moreover, several unfocused waves are usually transmitted for spatial coherent compounding to achieve higher image quality. Unfocused wave transmit includes plane wave transmit on linear array and diverging wave (DW) transmit on phased array. DW transmit offers a potential method for high frame rate cardiac imaging [1,2]. Using DW transmit or diverging wave compounding (DWC), many studies focus on estimating subtle movements to analyze complex mechanism in cardiac phases [3,4] or on exploring new diagnostic information, e.g., electromechanical wave to understand cardiac electromechanical coupling [5] and shear wave to quantify myocardial elasticity [6–9]. Compared with conventional focused imaging, DW or DWC imaging obtains high temporal resolution, but suffers from low signal-to-noise ratio (SNR) and penetration depth because of unfocused waves transmit, which hinders its applications.

Hadamard spatial coding [10,11] is designed to increase the SNR for synthetic transmit aperture (STA) beamforming and achieves an SNR gain of  $10 \log(M)$  dB, where  $M$  is the number of simultaneous active elements in STA. The data corresponding to each STA firing (with one element transmitting and all elements receiving) can be retrieved from spatial decoding using the inverse Hadamard matrix. Recently, Hadamard encoding has been applied to plane wave or diverging wave applications to increase the SNR for high frame rate imaging [12,13]. However, Hadamard decoding will be impaired when large motion exists. So when tissue motion is involved, the number of transmits is typically restricted to a small number, which limits the performance of Hadamard encoding.

Another way to increase the SNR is coded excitation, which relies on long pulse transmit to carry more energy along with pulse-compression to recover the spatial resolution [11,14–18]. Usually, the SNR gain is in proportion to the pulse length [15]. Coded excitation has been developed to achieve higher SNR, larger penetration depth and even higher frame rate for STA [19–22]. In our previous study, we have demonstrated the feasibility of coded excitation using chirp signal and Golay code to increase the SNR, contrast and penetration depth for DW/DWC imaging [23]. One drawback of Golay code is the need of two firings to

\* Corresponding author.

E-mail address: [luo.jianwen@tsinghua.edu.cn](mailto:luo.jianwen@tsinghua.edu.cn) (J. Luo).

transmit the complementary pairs for decoding, and thus the effective gain in frame rate will be compromised by a factor of 2. The orthogonal Golay codes have been used to encode pairs of focal zones so as to recover the decreased frame rate for focused imaging [14,22]. Orthogonal Golay codes have also been applied to STA imaging for firing multiple elements to achieve higher frame rate [22,24].

In this study, we present the spatio-temporal encoding method using orthogonal Golay pairs (OGPs-coded) for DWC imaging. Two pairs of orthogonal Golay codes are chosen. The second pair is designed to be the corresponding complementary set of the first pair. Each pair of orthogonal codes can be used to fire two DWs from two virtual sources simultaneously as their orthogonality ensures the separation of two simultaneously transmitted DWs. For the pulse compression, the two pairs need to be used in two consecutive transmit events. By using the orthogonal and complementary properties of Golay codes, two DWs can be obtained for compounding using two transmit events in the proposed OGPs-coded DWC method, whereas four transmit events are needed in the previous Golay coded method. The problem of decreased frame rate when using Golay coded excitation will be solved. Hereto, the feasibility and advantages of OGPs-coded DWC imaging will be investigated. Furthermore, because the decoding of Golay codes involves summing up the corresponding radio-frequency (RF) data coded by complementary pairs for range lobe cancellation, the effect of motion on Golay decoding for OGPs-coded DWC will also be studied.

## 2. Methods

A 64-element phased array transducer with a center frequency of 2 MHz, a pitch of 0.34 mm and a -6 dB bandwidth of 85% was used in this study. All the data post-processing of the simulations and experiments were performed in Matlab 2015 (The MathWorks, Inc., Natick, MA, USA).

Multiple steered DWs corresponding to different virtual sources behind the probe were transmitted for spatial coherent compounding in this study. As illustrated in Fig. 1, for non-steered DW, the virtual source was set behind the center of the probe with a distance equal to half aperture size (i.e., 10 mm) to cover all elements with a 90° scan sector, while for steered DW, multiple virtual sources were moving along a semi-circle (center: the center of the probe, radius: half aperture size) to different steering angles with respect to the vertical axis. The maximum steering angle was set as  $\pm 20^\circ$  [23]. DWC with a number in its front stood for coherent compounding using the specific number of DWs in this work. For example, 2DWC represents DWC with 2 steered DWs.

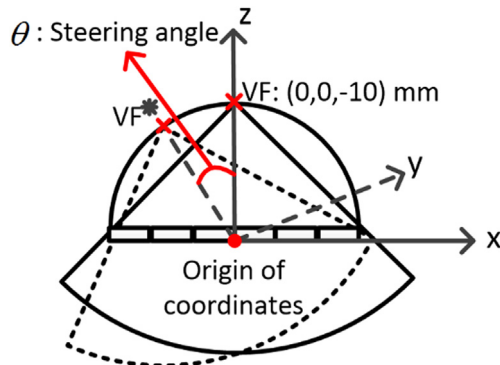


Fig. 1. Illustration of steered DW for spatial coherent compounding. VF and VF\* stand for the virtual sources for non-steered DW and steered DW in angle of  $\theta$ , respectively.

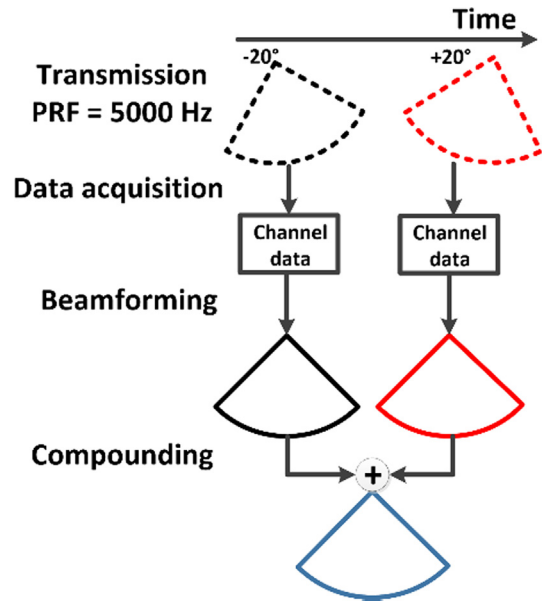


Fig. 2. Imaging sequence for 2DWC without coded excitation.

### 2.1. Imaging sequence design

#### 2.1.1. Non-coded DWC sequence

As an example, the sequence of 2DWC with steering angles of  $\pm 20^\circ$  is illustrated in Fig. 2. DWs in steering angles of  $\pm 20^\circ$  were transmitted sequentially, and the channel data were acquired and beamformed using delay-and-sum (DAS). DWC was performed by summing up the two post-beamformed RF frames corresponding to the two steering angles. It should be noticed that the non-coded DWC scheme used short pulse for excitation, which consists of 1.5 sinusoidal cycles at the center frequency of the probe.

#### 2.1.2. Orthogonal Golay pairs coded (OGPs-coded) DWC sequence

A typical sequence for 2DWC with Golay coded excitation proposed in our previous study [23] is shown in Fig. 3(a). A complementary pair A1 (+1, +1, +1, -1) and B1 (+1, +1, -1, +1) was used. In the first and second transmit events, DWs in steering angle of  $-20^\circ$  were transmitted, coded with A1 and B1, respectively. In the third and fourth transmit events, DWs in steering angle of  $+20^\circ$  coded by A1 and B1 respectively were transmitted. After the four channel datasets corresponding to the two steering angles coded by the complementary pairs respectively were obtained, beamforming was performed using DAS followed by the decoding procedure. Firstly, convolution of the post-beamformed RF data with the matched filter (MF) corresponding to the codes for firing (MF(A1) or MF(B1)) was performed, then each two filtered RF frames coded by the complementary pair with the same steering angle were summed up to obtain an RF frame with recovered axial resolution. Finally, DWC was performed by summing up the two RF frames with different steering angles.

In the proposed OGPs-coded DWC sequence, two pairs of orthogonal Golay codes A1 (+1, +1, +1, -1), A2 (+1, -1, +1, +1) and B1 (+1, +1, -1, +1), B2 (+1, -1, -1, -1) were chosen. A1 and A2, as well as B1 and B2, were orthogonal. B1 and B2 were the corresponding complementary sets of A1 and A2. A typical OGPs-coded sequence for 2DWC is shown in Fig. 3(b). In the first transmit event, A1 and A2 were used to implement the spatial encoding for two virtual sources to transmit DWs in two steering angles of  $\pm 20^\circ$  simultaneously. Next, DWs in the same two steering angles coded by B1 and B2 respectively were transmitted simultaneously. Beamforming was performed on the acquired channel data based on the different virtual sources. The orthogonality of Golay codes ensured the separation of the two

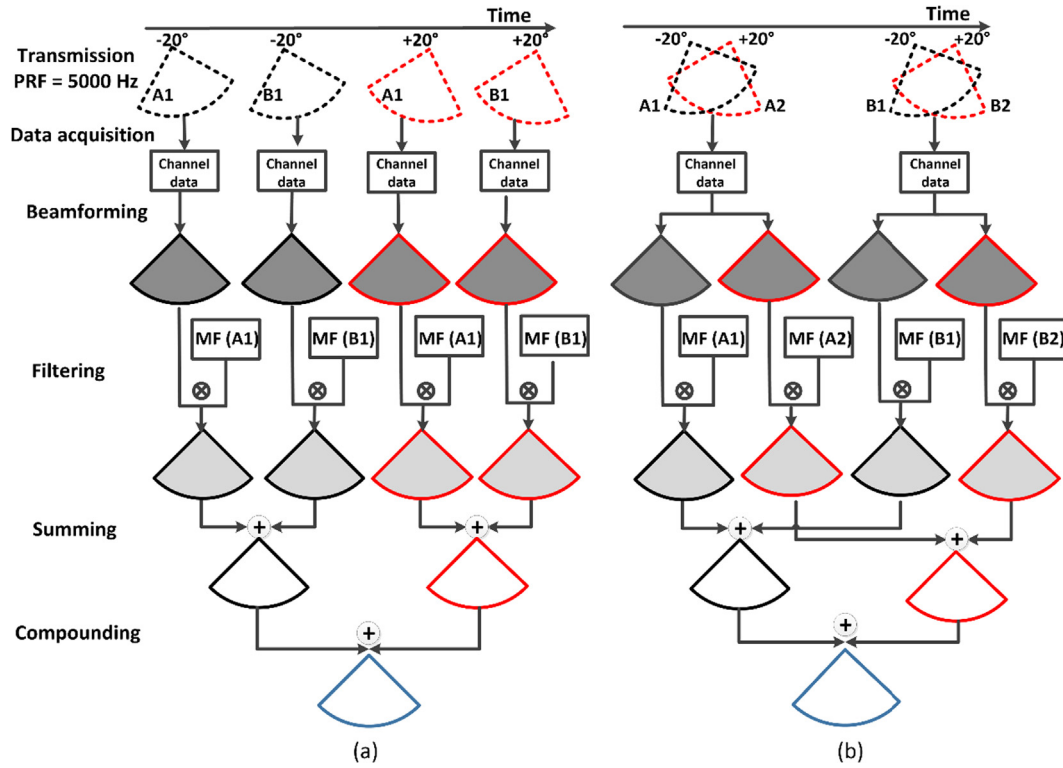


Fig. 3. Imaging sequences for (a) complementary Golay-coded 2DWC and (b) the proposed OGPs-coded 2DWC. A1 and B1, as well as A2 and B2, are complementary Golay pairs, while A1 and A2, as well as B1 and B2, are orthogonal Golay pairs.

simultaneously transmitted DWs when convolution of the post-beamformed RF data with the matched filter was performed. Summing up each two filtered RF frames coded by the complementary Golay pair produced an RF frame with recovered axial resolution corresponding to one steering angle. Finally, the two frames with different steering angles were obtained and summed for DWC. Compared with the complementary Golay-coded DWC sequence, the proposed OGPs-coded DWC sequence transmitted 2 DWs simultaneously, thus compensating the frame rate reduction caused by transmissions of complementary codes.

In this study, we mainly contrasted the performance of the proposed imaging scheme to that of the non-coded scheme at the same frame rate. By using the similar transmission strategy, more DWs with different steering angles could be transmitted for coherent compounding in both the non-coded and OGPs-coded sequences. For the OGPs-coded DWC scheme, 2 DWs coded by the chosen orthogonal Golay pair respectively were always transmitted simultaneously, so even numbers of compounding angles were tested for DWC in this study. 8 angles were set ranging from  $-20^\circ$  to  $-2.5^\circ$  with an interval of  $2.5^\circ$ . For each steering angle  $\theta$ , the corresponding paired steering angle was  $\theta + 22.5^\circ$ . Specifically, for 2DWC, the steering angles of  $-20^\circ$  and  $2.5^\circ$  ( $= -20^\circ + 22.5^\circ$ ) were used, while for 4DWC, another two steering angles of  $-17.5^\circ$  and  $5^\circ$  ( $= -17.5^\circ + 22.5^\circ$ ) were used in addition to the two steering angles for 2DWC. More steering angles were set in a similar manner. Finally, these steering angles were distributed uniformly within  $\pm 20^\circ$  excluding  $0^\circ$ , and each pair of steering angles has the same opening angle of  $22.5^\circ$ . The maximum number of compounding angles was 16.

### 2.1.3. Single-line transmit imaging

Conventional focused imaging using single-line transmit (SLT) was involved as a reference. Focused beam was transmitted line-by-line by 180 times, obtaining 180 beamformed lines in  $90^\circ$  sector view. The transmit focal depth was 80 mm.

For all the imaging sequences, full aperture and Tukey window

( $\alpha = 0.5$ ) were used for both transmit and receive. The sampling frequency of the channel data was set as 50 MHz. Dynamic focusing with an F-number of 2 was used and the pulse repetition frequency was set as 5 kHz. For DW imaging schemes, 180 imaging lines were beamformed in  $90^\circ$  sector view.

## 2.2. Simulations

Point target and tissue phantom simulations were considered in Field II [25,26]. The attenuation was ignored in the simulations. To simulate the noisy environment, Gaussian white noise with the same energy (10 dB for non-coded 1DW) was added to the channel data in different imaging schemes.

### 2.2.1. Simulations of point targets

In order to test the feasibility of the OGPs-coded DWC sequence, five point targets at different depths (30–110 mm) were simulated, which were 20 mm apart from each other at the azimuthal central axis of the field-of-view. The spatial resolutions in the axial and lateral directions respectively were evaluated. As illustrated in Fig. 4, the normalized axial and lateral profiles of a point target with different imaging schemes were extracted firstly, and the axial and lateral beam widths were quantified by measuring the width of main lobes defined by  $-6$  dB value [27], which are related to the spatial resolution in the corresponding directions.

### 2.2.2. Simulations of tissue phantoms

To study the performance of different imaging schemes on B-mode images, a static tissue phantom with dimensions of  $60 \times 50 \times 5 \text{ mm}^3$  (axially  $\times$  laterally  $\times$  elevationally) was simulated. The phantom consisted of randomly distributed scatterers with a density of  $25 \text{ mm}^{-3}$  and a scattering intensity following Gaussian distribution. The phantom consisted of a spherical cystic region with a diameter of 20 mm and zero scattering intensity (Fig. 7). To study the effect of motion, tissue phantom in moving states was also tested for different imaging

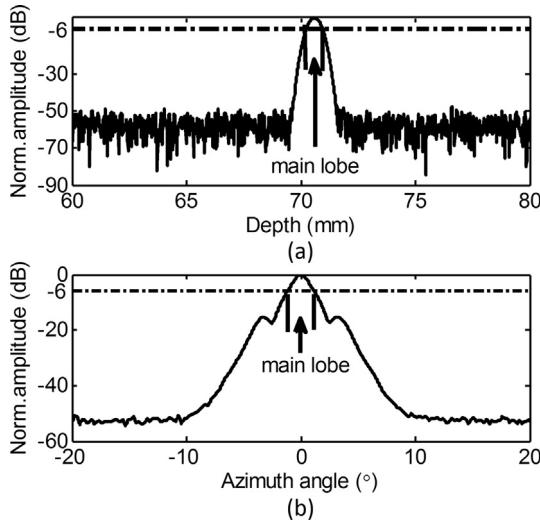


Fig. 4. Example of a PSF profile in the (a) axial and (b) lateral directions.

schemes. The moving speed was set as 15 cm/s, which was the maximum velocity according to the normal and physiological longitudinal myocardial velocities range [1]. The moving direction was along 45° downward from the horizontal direction. The moving phantom was not tested for the SLT scheme as SLT for the static phantom was used as reference.

The image quality of the OGPs-coded scheme is contrasted to those of the non-coded DWC and SLT schemes. The evaluation metrics for the tissue phantoms included the SNR and contrast ratio (CR). For each imaging scheme, 20 randomly generated noise datasets were added to the channel data of the phantoms to simulate 20 datasets with fixed ultrasound data and random noise. The SNR was defined as the ratio of the mean and standard deviation of 20 envelope datasets for each A-line along the depth. The SNRs of 11 neighboring A-lines centered at a specified A-line were averaged [13]. The CR was quantified by the average cyst-to-background brightness difference [23], and the regions of interest (ROIs) for CR quantification were marked as circles in Fig. 7 (radius of ROIs = 7 mm).

### 2.3. Experimental validation

To investigate the performance of the OGPs-coded DWC scheme in experimental condition, phantom experiments and preliminary *in vivo*

experiments were performed on a ULA-OP system [28] which supports the arbitrary waveform design to implement simultaneous transmission of multiple DWs. This system was equipped with a 128-elements phased array (PA230, Esaote SpA, Florence, Italy). The center frequency is 2 MHz and pitch is 170  $\mu\text{m}$ . Because the system has only 64 independent channels, the odd elements of the probe were used. The effective pitch was 340  $\mu\text{m}$ , the same as that in the simulations. The acquisition parameters were also the same as those used in the simulations. All images were acquired at the same peak-to-peak voltage level of 24 volts and with the same time gain compensation (TGC) of 7  $\text{dB cm}^{-1}$ . In the experiments, the involved sequences were programmed to execute sequentially so that the same location and view were scanned. The channel data of the three schemes were obtained all at once.

#### 2.3.1. Phantom experiments

The proposed method was tested on a tissue-mimicking phantom (model 040GSE, CIRS Inc., Norfolk, VA, 0.5  $\text{dB/MHz/cm}$ ). For the phantom experiments, three imaging schemes were tested using even numbers of compounding angles, i.e., the non-coded, OGPs-coded and SLT schemes. The normalized axial and lateral profiles of a wire (indicated with the arrow in Fig. 11) in different imaging schemes were extracted for quantification of the axial and lateral beam widths. Another two evaluation metrics for the phantom experiments were the SNR and CR, which were calculated in the same way as that in the simulations. The radius of the ROIs (shown in red dashed circles in Fig. 11) for CR quantification was 3.5 mm.

#### 2.3.2. *In vivo* experiments

A healthy male volunteer was involved for the *in vivo* study. Data were acquired from apical four chamber view and short axis view using non-coded, OGPs-coded and SLT schemes, respectively. For the non-coded and OGPs-coded schemes, 8 DWs and 12 DWs were used for compounding in the apical four-chamber view and short axis view, respectively. To contrast the image quality for the *in vivo* study, we acquired the ECG signals to select the images of different sequences corresponding to the same cardiac phase. This study was approved by the institutional review board of Tsinghua University and written informed consent was obtained from the subject.

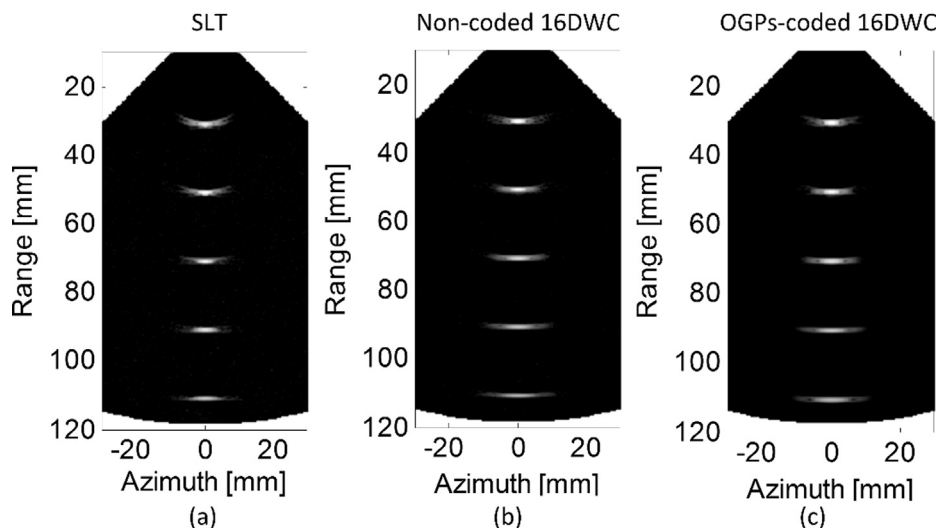
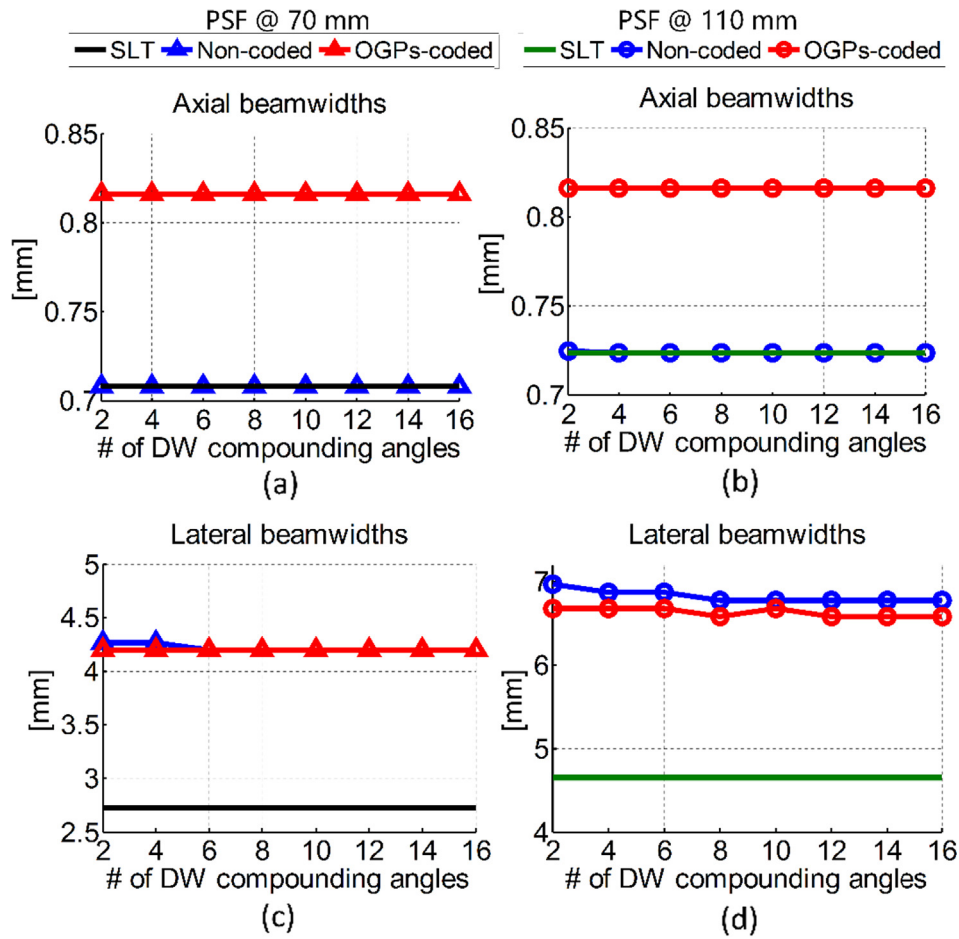


Fig. 5. The PSFs of the three imaging schemes. (a) SLT, (b) non-coded 16DWC, (c) OGPs-coded 16DWC. The display dynamic range is 55 dB.





**Fig. 6.** Quantitative characteristics of the PSFs at depth of 70 mm including the (a) axial beam widths and (c) lateral beam widths for different imaging modes. Quantitative characteristics of the PSFs at depth of 110 mm including the (b) axial beam widths and (d) lateral beam widths for different imaging modes.

### 3. Results

#### 3.1. Simulations of point targets

The PSFs of the SLT, non-coded 16DWC and OGPs-coded 16DWC imaging schemes are shown in Fig. 5. As expected, the lateral resolution of the DWC scheme is lower than that of SLT. Visually, the OGPs-coded scheme performs comparably to the non-coded scheme regarding the spatial resolution in both the axial and lateral directions.

Fig. 6 show the quantitative axial and lateral beam widths of the PSFs at depths of 70 mm and 110 mm respectively for different imaging schemes. The values for the SLT scheme are indicated by the horizontal lines as references (the same for other figures). With different numbers of compounding angles, the non-coded obtains the same axial beam widths as the SLT scheme, while the OGPs-coded scheme obtains larger axial beam widths compared with the non-coded scheme and SLT. At depth of 70 mm, the OGPs-coded scheme obtains the same lateral beam widths as the non-coded one with different numbers of compounding angles, while at depth of 110 mm, the OGPs-coded scheme obtains narrower lateral beam widths than the non-coded one. For PSFs at both 70 mm and 110 mm, SLT obtains the narrowest lateral beam widths among all imaging sequences.

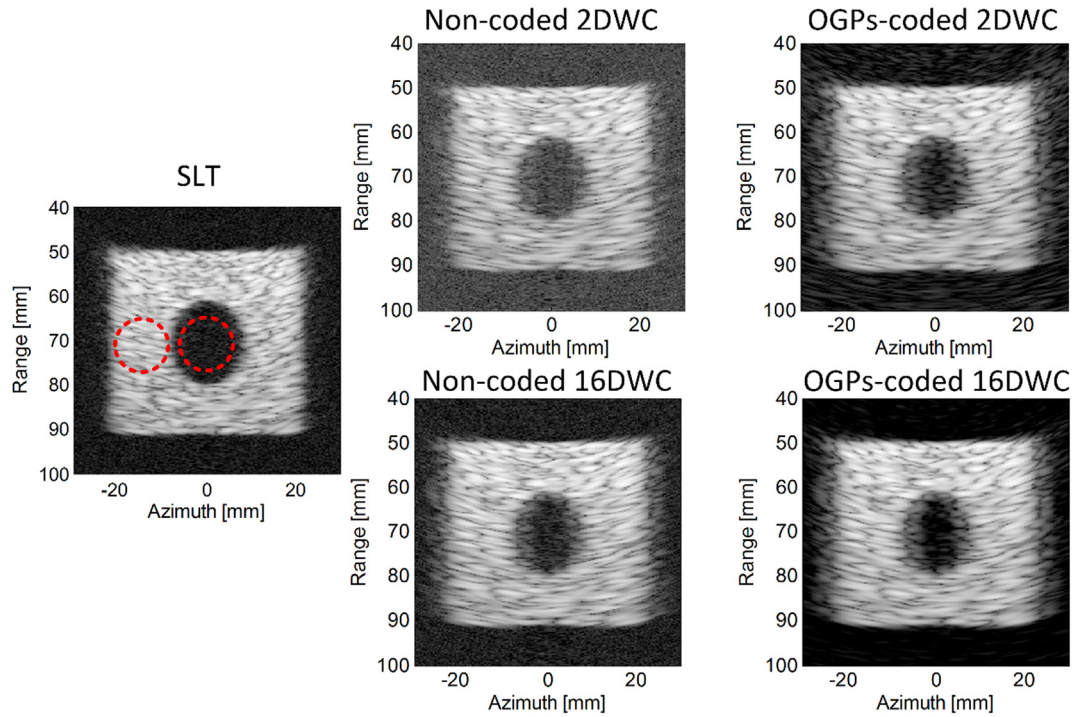
#### 3.2. Simulations of static phantom

Fig. 7 shows the B-mode images of the simulated static phantom obtained from SLT, the non-coded 2DWC and 16DWC schemes, and the OGPs-coded 2DWC and 16DWC schemes, respectively. As expected, 16DWC reduces the noise more significantly than 2DWC. With the same

number of DWs, the OGPs-coded scheme shows less noise in the entire field-of-view compared with the non-coded scheme. The SLT scheme shows the best contrast. However, more noise in the cystic region is observed in SLT than in OGPs-coded 16DWC.

To quantitatively analyze the performance of different imaging schemes in the phantom simulations, the CR and SNR values for different imaging schemes are shown in Fig. 8. For the CR performance (Fig. 8(a)), using more DWs for compounding obtains higher contrast for both the non-coded and OGPs-coded schemes. The OGPs-coded DWC scheme performs better than the non-coded scheme, and the contrast gain is 3–4 dB with different numbers of compounding angles. With an increased number of compounding angles, the contrast gain by the OGPs-coded scheme decreases. SLT performs the best, with a CR gain of 2.5 dB compared with OGPs-coded 16DWC.

Fig. 8(b) and (c) show the quantitative SNR values for 2DWC and 16DWC respectively. The central A-line for SNR quantification is selected at the lateral location of 16 mm (also applied for the results of moving phantom simulations below). The SNRs of 2DWC and 16DWC with and without coded excitation are plotted along the depth, with the SNR of SLT as the reference. It shows that 16DWC achieves an SNR gain of 5 dB compared with 2DWC for both the non-coded and OGPs-coded schemes. OGPs-coded DWC performs better than non-coded DWC with an SNR gain of 8–10 dB. The SLT scheme achieves an SNR of 25 dB. It outperforms the non-coded schemes with an SNR gain of 7 dB in 2DWC and 2 dB in 16DWC, but performs worse than the OGPs-coded ones with an SNR reduction of 1.5 dB in 2DWC and 7 dB in 16DWC.



**Fig. 7.** B-mode images of the simulated tissue phantom in static state obtained by different imaging schemes. The display dynamic range is 55 dB. The red circles indicate the ROIs for CR quantification.

### 3.3. Simulations of moving phantom

Fig. 9 shows the B-mode images of the simulated moving phantom obtained from 8DWC and 12DWC with and without coded excitation respectively. With the same number of DWs, the OGP-coded scheme outperforms the non-coded one with less noise on the B-mode images. The SLT image of the static phantom is shown as the reference, which obtains the highest contrast between the cyst and background.

Fig. 10 shows the corresponding CR and SNR results for different imaging schemes. As the number of compounding angles increases, the CR increases first and then decreases for both the non-coded and OGP-coded schemes. Furthermore, the OGP-coded scheme shows a faster decline than the non-coded scheme when using too many DWs for compounding. For the moving phantom, in order to achieve high contrast, the number of compounding angles is suggested to be small than to a specific value, i.e., 8 for the non-coded scheme, and 12 for the

OGPs-coded scheme. With 2–16 compounding angles, the OGP-coded scheme outperforms the non-coded scheme, with a CR gain of 3–4.5 dB. Compared with the CR results of the static phantom in Fig. 8(a), the CRs of moving phantom are lower for both the non-coded and OGP-coded schemes.

For the SNR performance, SLT still outperforms the non-coded scheme, but performs worse than the OGP-coded scheme. The SNRs of 12DWC are lower than those of 8DWC for both the non-coded and OGP-coded schemes. Nevertheless, OGP-coded scheme performs better than the non-coded one with an SNR gain of 9 dB for 8DWC and 7.5 dB for 12DWC.

### 3.4. Phantom experiments

Fig. 11 shows the B-mode images of the tissue-mimicking phantom using SLT, the non-coded and OGP-coded schemes, respectively. For

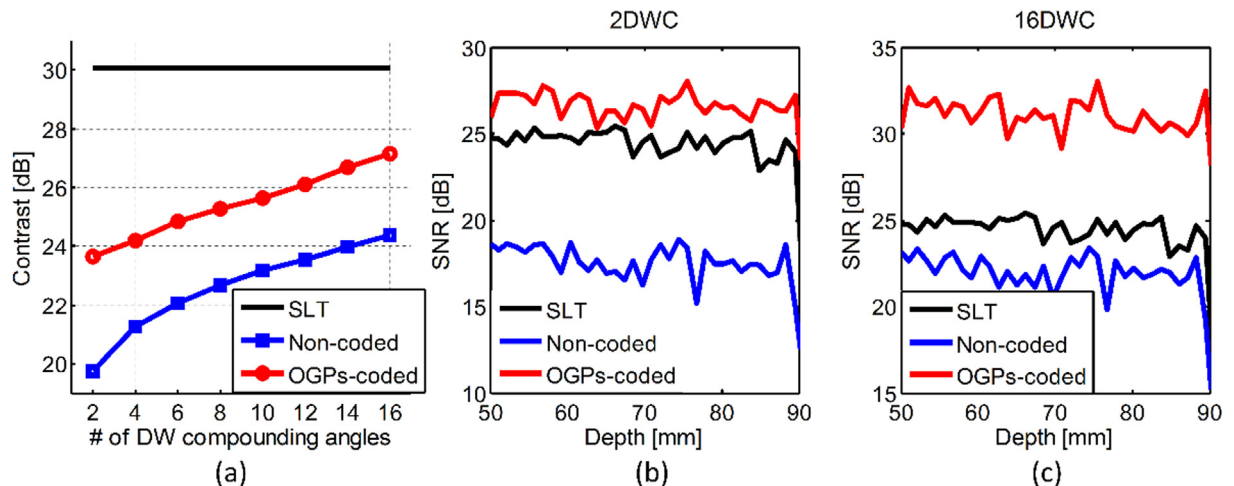


**Fig. 8.** Quantitative analysis of the simulated tissue phantom in static state for different imaging schemes including SLT, non-coded and OGP-coded DWC. (a) Contrast, (b) SNR for 2DWC and (c) SNR for 16DWC.

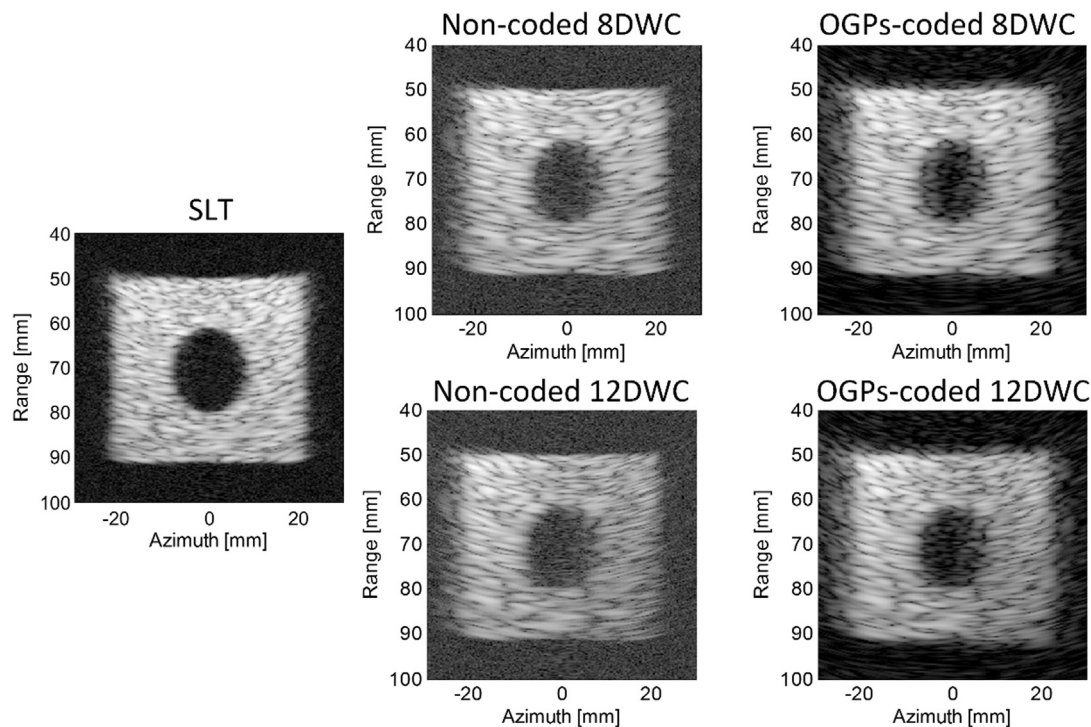


**Fig. 9.** B-mode images of the simulated tissue phantom in moving state obtained by non-coded 8DWC and 12DWC, OGP-coded 8DWC and 12DWC, respectively. B-mode image of static tissue phantom obtained by SLT is shown as a reference. The display dynamic range is 55 dB.

both 8DWC and 12DWC, the OGP-coded scheme obtains higher contrast between the cyst and background at the depth of 100 mm when compared with the non-coded scheme. SLT performs the best with the highest intensity in the background and the lowest intensity in the cyst.

The quantitative axial and lateral beam widths for a wire (indicated by the arrow in Fig. 11) was calculated and shown in Fig. 12. Compared with the non-coded and SLT schemes, the OGP-coded modes obtain slightly worse axial resolutions with different numbers of DW compounding angles. The lateral resolutions are almost the same for the non-coded and OGP-coded modes. SLT achieves the smallest main lobe width in lateral direction.

The CR results of the non-coded and OGP-coded schemes with different compounding angles as well as the SLT scheme are shown in Fig. 13(a). The OGP-coded scheme achieves higher contrast with a gain of 1–2 dB compared with the non-coded one. The CR gains decrease as the number of compounding angles increases. When using

16DWC, the non-coded scheme obtains a slightly higher contrast compared with the OGP-coded scheme. The SLT scheme obtains the highest CR value of 17.2 dB. Compared with 16DWC, SLT achieves a CR gain of about 3 dB.

The SNRs as a function of depth for the non-coded and OGP-coded schemes with 8DWC and 12DWC respectively as well as the SLT scheme are shown in Fig. 13(b) and (c). The central A-line for SNR quantification is located in the middle of the phantom. The SNRs decrease with the depth for all the imaging schemes. The OGP-coded scheme achieves SNR gains of 3–6 dB compared with the non-coded one. When using 8DWC, the non-coded scheme obtains 2 dB lower SNR than SLT, while when using 12DWC, the non-coded scheme obtains similar SNR values to SLT. The OGP-coded scheme achieves higher SNR with a gain of 2–5 dB than SLT with 8DWC and 12DWC.

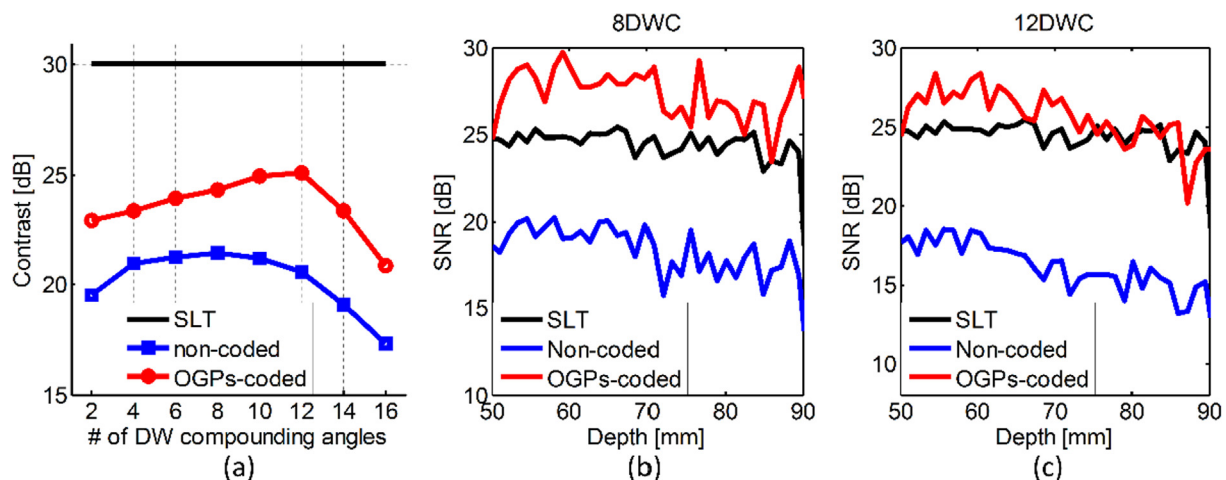


**Fig. 10.** Quantitative analysis of the simulated tissue phantom in moving state for different imaging schemes including non-coded and OGP-coded DW. The results of SLT for static phantom are shown as the reference. (a) Contrast, (b) SNR for 8DWC and (c) SNR for 12DWC.



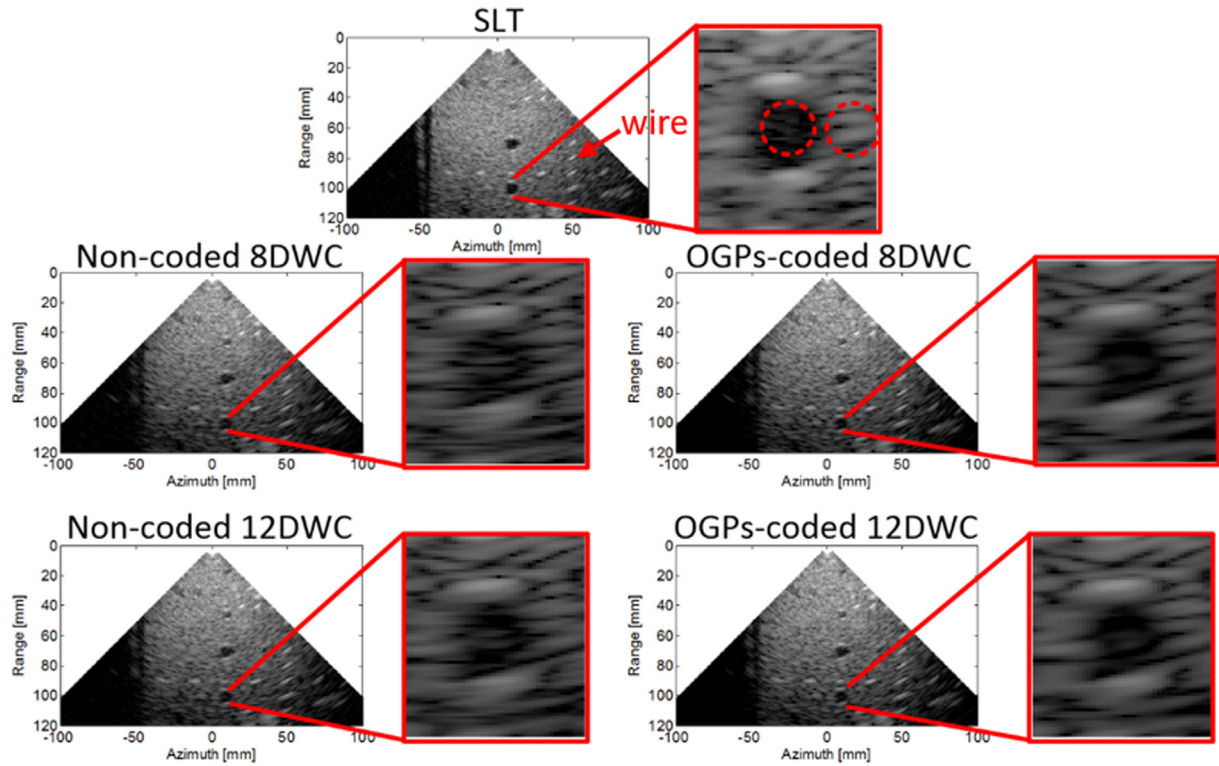


Fig. 11. B-mode images of the tissue-mimicking phantom obtained by different imaging schemes, including SLT, non-coded and OGPs-coded DWC. Zoomed-in views of the cyst at depth of 100 mm are shown in red blocks respectively. The display dynamic range is 60 dB. The red dashed circles indicate the ROIs for CR quantification.

### 3.5. In vivo experiments

Cardiac images acquired by different imaging schemes are shown in Fig. 14 for qualitative assessment for the *in vivo* study. The images are in the end-diastolic phase selected from different imaging schemes based on the ECG signals. The images acquired by the SLT scheme are shown as references. The OGPs-coded scheme obtains higher image intensity than the non-coded one, in mitral valve (MV), septal wall and lateral wall of the left ventricle (LV) as indicated by the arrows. Compared with the non-coded scheme, the OGPs-coded scheme obtains more myocardial structures that are similar to those shown in the SLT scheme.

## 4. Discussion

Our previous study has proved the feasibility of Golay coded

excitation in obtaining better image quality for DWC imaging [23]. However, the frame rate is decreased by 2 folds compared with non-coded DWC, because of the need for two firings to transmit the complementary codes. In this paper, a spatio-temporal encoding method using two pairs of orthogonal Golay codes for DWC is proposed. Two virtual sources are spatially encoded by the first pair of orthogonal Golay codes to transmit two DWs simultaneously in the first transmit event. As the corresponding complementary set of the first pair, the second pair is used in the same manner in the following transmit event for Golay decoding. The two DWs from two virtual sources can easily be separated and compressed based on the orthogonal and complementary properties of the two pairs of orthogonal Golay codes. The frame rate will be recovered, thanks to the simultaneous transmission of two DWs. The feasibility of this method is tested in simulations, phantom experiments and preliminary *in vivo* experiments. The effective separation and compression of the two simultaneously transmitted DWs are

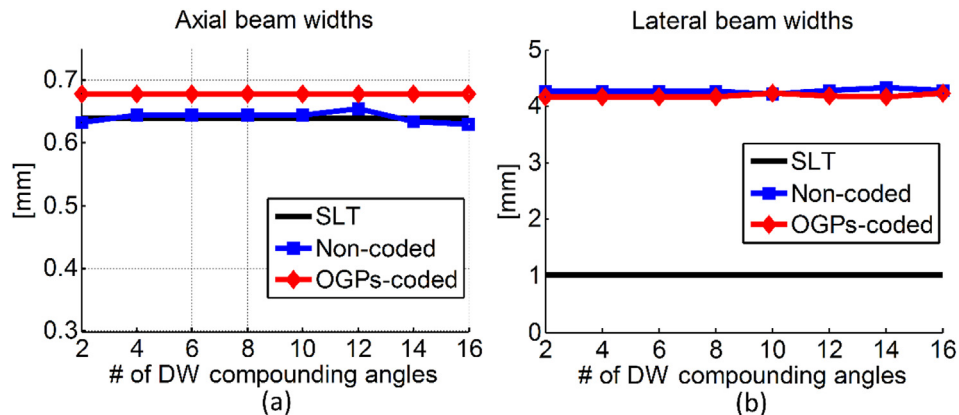
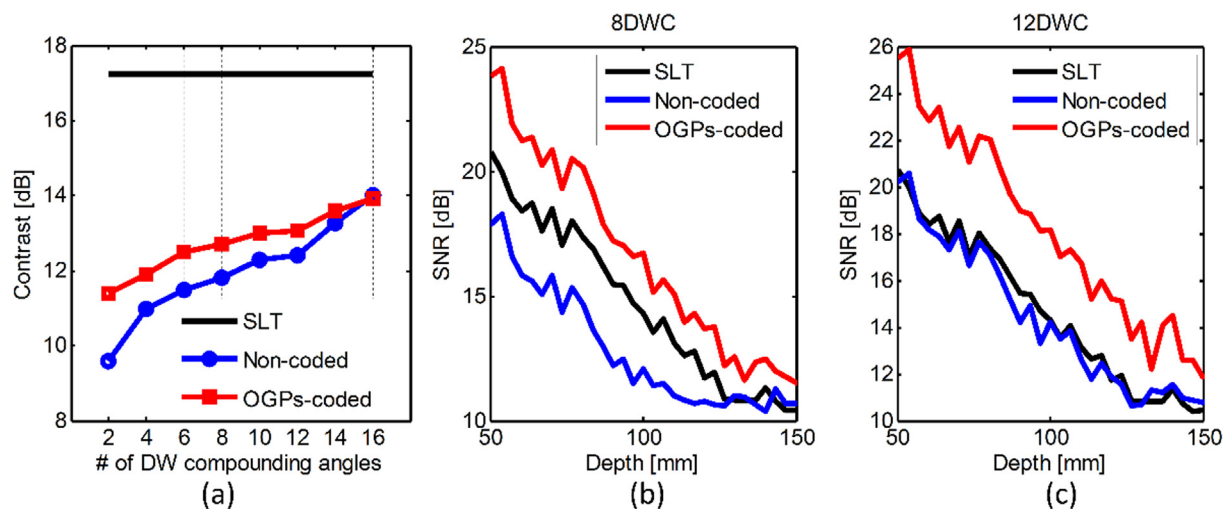


Fig. 12. The quantitative (a) axial and (b) lateral beam widths from different modes for a wire (indicated by arrow in Fig. 11) in experiment.





**Fig. 13.** Quantitative analysis of phantom experiments for different imaging schemes including SLT, non-coded and OGPs-coded DWC. (a) Contrast, (b) SNR for 8DWC and (c) SNR for 12DWC.

demonstrated. The results of both the simulations and phantom experiments validate that the proposed OGPs-coded scheme achieves higher SNR and contrast than non-coded DWC. The *in vivo* study shows clearer myocardium in the OGPs-coded scheme than in the non-coded one.

According to the PSF simulation results presented in Fig. 6 and experimental results presented in Fig. 12, SLT obtains the narrowest lateral beam width because of the focused beam transmit. By contrast, the DWC schemes obtain larger beam widths due to the unfocused wave transmit. The OGPs-coded DWC scheme obtains slightly larger axial beam widths than the non-coded DWC scheme. Almost the same lateral beam widths are obtained in the OGPs-coded and non-coded schemes. These results are consistent with our previous findings using complementary Golay codes for DWC [23]. This demonstrates that the simultaneously transmitted DWs in different steering angles with the OGPs-coded method can be separated and decoded effectively. Most

importantly, the OGPs-coded scheme maintains the frame rate of the non-coded scheme, and thus overcomes the limitation of Golay coded excitation in frame rate.

The results of the static phantom simulations show that the OGPs-coded scheme obtains higher SNRs and higher CRs than the non-coded one (Fig. 8). The SNRs and CRs increase with the number of compounding angles for both the non-coded and OGPs-coded schemes (Fig. 8). Correspondingly, the results of the phantom experiments validate that the OGPs-coded scheme outperforms the non-coded scheme in terms of SNR and contrast (Figs. 11 and 13). Higher SNRs and CRs are achieved with a larger number of compounding angles for both the non-coded and OGPs-coded schemes. It should be noted that the SNR and CR gains by the OGPs-coded scheme in the phantom experiments are smaller than those in the simulations. One possible reason is that noise in the experiments is more complicated than the random additive white noise used in the simulations. Another reason is that acoustic

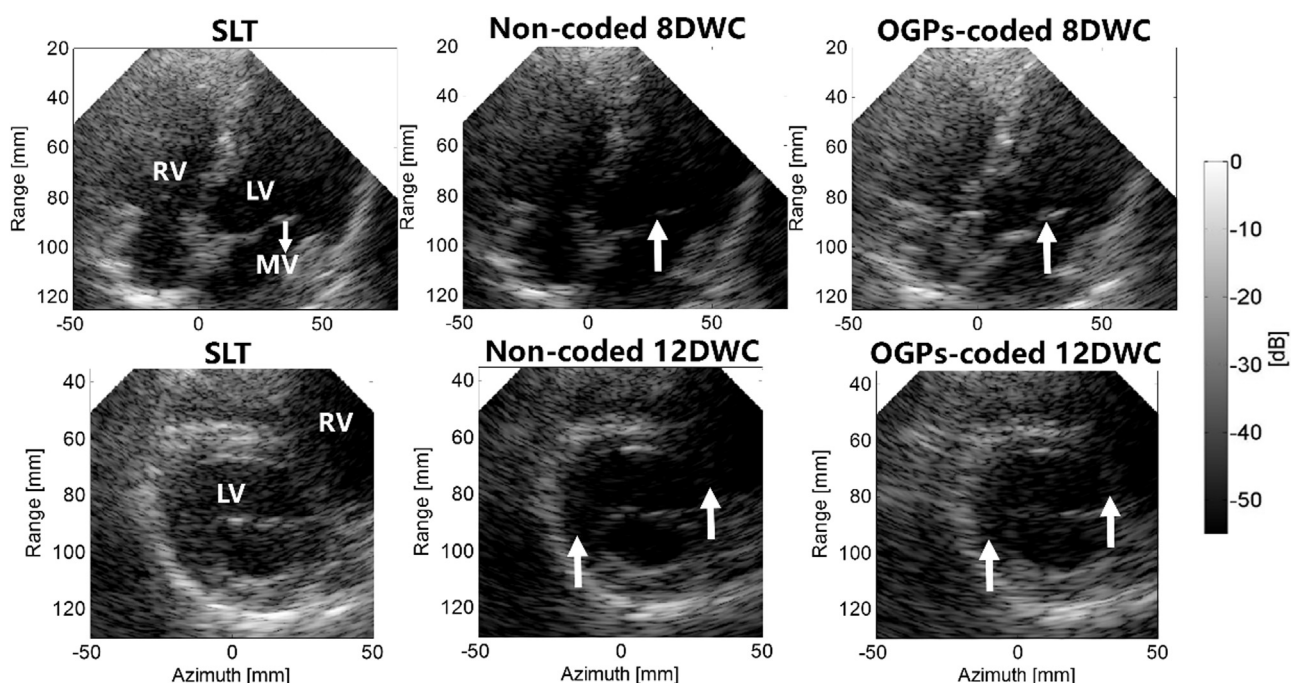


**Fig. 14.** *In vivo* images of the left ventricle of a healthy volunteer in the apical four chamber view (upper panel) and short axis views (lower panel) acquired from different imaging sequences.

attenuation is ignored in the simulations but exists in the experiments. Accordingly, the SNR is relatively unvaried in the simulations (Figs. 8 and 10) but decreases with the depth in the phantom experiments (Fig. 13). The attenuation causes frequency shift leading to incomplete elimination of the range lobes in the OGPs-coded scheme [15]. Therefore, the performance of the OGPs-coded scheme is expected to be impaired in experimental conditions. Moreover, the CR analysis of the static phantom simulations shows that using 16 DWs for compounding, the non-coded scheme still obtains lower contrast than the OGPs-coded scheme (Fig. 8). However, in the phantom experiment (Fig. 13), using 16 DWs, the non-coded scheme achieves slightly higher contrast than the OGPs-coded scheme. It means that at attenuated medium and with too many compounding angles, the advantages of the proposed scheme will be lost. The impaired performance of the OGPs-coded scheme in the experiments compared with that in the simulations is also in agreement with the results of our previous study using complementary Golay codes [23].

When using the OGPs-coded method, the theoretical improvement in SNR is  $10 \times \log(N \times M \times TB)$ , where  $N$  is the number of transmit events corresponding to each steering angle,  $M$  is the number of simultaneously transmitted DWs, and  $TB$  is the time-bandwidth product of the codes, which is equal to the length of the code ( $L$ ) for Golay codes [11,15,16]. For the proposed method, when  $N = 2$ ,  $M = 2$  and  $L = 4$ , the theoretical improvement in SNR will be  $10 \times \log(2 \times 2 \times 4) = 12$  dB. The SNR gains in the simulations are slightly lower than the theoretical value (Fig. 8), possibly owing to the transfer function (i.e., band-pass response) of the transducer. In the phantom experiments, the SNR gains are expected to be lower than the theoretical value considering the effects of transducer transfer function, frequency shift and more complex experimental conditions (Fig. 13).

Spatial coherent compounding is usually adopted to improve the image quality of DW imaging. Our simulation and experimental results for the static phantom validate the feasibility of DWC in improving the imaging contrast and SNR for both the OGPs-coded and non-coded schemes (Figs. 7, 8, 11 and 13). However, when large motion exists during transmissions of multiple DWs, the maximum number of compounding angles will be limited for both the OGPs-coded and non-coded schemes, considering the motion artifacts when too many DWs are compounded (Fig. 10). It should be noticed that for the OGPs-coded DWC scheme, motion artifacts also appear due to imperfect cancellation of range lobes in decoding as motion between the two transmits destroys the complementarity condition for Golay coded excitation. Furthermore, this motion degradation will be accumulated as the number of compounding angles increases in the OGPs-coded scheme.

In this study, the motion artifacts from DWC for the OGPs-coded and non-coded schemes are in the same condition because of the same frame rate achieved. However, the results of the simulated phantom moving at 15 cm/s (Figs. 9 and 10) show that with less than 16 DWs, the OGPs-coded scheme outperforms the non-coded scheme, indicating that for DW transmit with low energy, it is still recommended to use Golay coded excitation to carry more energy for image quality improvement, although Golay codes have the potential issue of incomplete decoding. For the simulated moving phantom, the quantitative CR values in Fig. 10(a) show a faster declining trend for the OGPs-coded scheme when more than 12 DWs are used for compounding. This validates the motion degradation accumulation with an increasing number of compounding angles in the OGPs-coded scheme. Hereto, it is not recommended to apply the Golay coded excitation when a too large number of compounding angles is used. Furthermore, motion compensation [29,30] may be used to solve the problem of motion degradation and improve the performance of the OGPs-coded scheme. The DWC imaging scheme is more sensitive to the axial motion (i.e., motion along the transmitted beam) than to the lateral motion (i.e., motion perpendicular to the transmitted beam), probably because of the higher resolution in the axial direction [29]. In the simulations of the moving phantom, the image quality of the right part of the phantom is more

degraded than that of the left part when more compounding angles are used, either without or with coded excitation (Fig. 9). This is because the moving direction is along  $45^\circ$  downward from the horizontal direction and the right part of the phantom undergoes a larger velocity component along the transmitted beam.

Overall, the results of the simulations and phantom experiments (Figs. 7–13) show that the non-coded scheme performs worse than SLT in terms of SNR and contrast due to the low energy and high side lobe levels with DW transmit. Compared with SLT, the proposed OGPs-coded DWC scheme obtains higher SNR because of longer pulse transmit (Figs. 7–13). For the static phantom, the image of OGPs-coded 16DWC shows obviously less noise in the cystic region than that of SLT (Fig. 7). However, the contrast of the OGPs-coded DWC scheme is lower than that of SLT (Figs. 7–13). This reveals the high side lobe levels with unfocused wave transmit in DWC. By compounding more DWs, we can achieve lower side lobe level, but at expense of lower frame rate. Moreover, an important issue to deal with is motion artifacts on the summation of multiple DWs [30,31].

The *in vivo* cardiac images in Fig. 14 show that the OGPs-coded scheme obtains brighter image intensity than the non-coded scheme, manifesting higher SNR. Comparing the proposed imaging scheme to SLT, some acoustic shadowing artifacts appear in the blood pool and surrounding tissues for the OGPs-coded scheme, probably brought by complex reverberation/clutter effects with high side lobe levels and cross-talks between the simultaneously transmitted DWs. In addition, although coded excitation for DW imaging has been proved to improve the quality of cardiac B-mode imaging, its performance in cardiac function analysis such as motion and deformation imaging remains to be investigated.

Our proposed method implements the spatio-temporal encoding for DWC using orthogonal Golay pairs. It aims to recover the decreased frame rate when using Golay codes due to the complementary codes transmitted for pulse compression. It should be noticed that, the Golay sequence is a special case of complementary sequences, with the number of sequences equal to 2. In general,  $M$  complementary sets that are mutually orthogonal can be created and be used to create more virtual sources during one transmit event to further improve the imaging SNR [22,32]. However, the thermal effects when more DWs are transmitted simultaneously and motion degradation during more transmit events should be considered. In this study, Orthogonal Golay codes of length 4 has been used. Golay codes of a longer length can be used to further improve the time-bandwidth-product (TBP) of coded excitation, which will achieve larger SNR gain and deeper penetration [15,16]. However, the axial resolution will be decreased as Golay codes of a longer length will narrow the fractional band [33]. Moreover, long pulse transmit has a high demand to the hardware of ultrasound systems. Optimization of the code length to best compromise the trade-off between SNR enhancement and spatial resolution will depend on different applications.

Hadamard encoding and coded excitation are both effective ways to increase the SNR. Hadamard encoding uses the Hadamard matrix for spatial coding, thus multiple elements can be activated simultaneously in STA or multiple virtual sources can be created in DWC. The simultaneous active waves carry more energy into the tissue to achieve higher SNR. Usually, it is desirable to limit the peak pressure amplitudes of the ultrasound wave interrogating the tissue, a delay is added between the simultaneously active waves in the Hadamard encoding method. The decoding process for the Hadamard encoding method is stable and easy to perform by simple additions and subtractions. However, for correct decoding, the delays added between the simultaneously active waves must be compensated, thus leading to the dead zone problem in the near field [12]. Coded excitation using chirp or Golay codes relies on long pulse transmit to carry more energy for higher SNR and filters for pulse compression. The frequency shift caused by attenuation will degrade the outcomes of pulse compression. Much effort on matched or mismatched filter design for the pulse

compression in coded excitation has been made [34–36]. Hadamard spatial encoding involves coding in the slow time domain, whereas coded excitation mainly in the fast time domain. Therefore, Hadamard encoding is more affected by the motion compared with coded excitation. Under situations with rapid motion, coded excitation may be a better solution than Hadamard encoding.

Golay coding obtains a higher SNR gain than chirp coding when there is no attenuation [15,23]. In attenuated medium, Golay coding is more sensitive to the frequency shift caused by attenuation, and therefore chirp coding outperforms Golay coding and achieves larger gains in contrast and SNR/penetration for DW imaging [23]. As discussed above, Golay coding also suffers from the motion degradation. However, a multi-level pulser is needed to provide better spectrum control for chirp signal, and the decoding filter is also more complex. Therefore, coded excitation with chirp signal has higher demand for the hardware. In contrast, a bi-level pulser is used for Golay coding at a much lower cost [14]. Golay codes have been shown to be comparable and even advantageous in certain applications [14]. In the future, the Golay-coded scheme can be further optimized, for example, using the mismatched filter with the consideration of the frequency shift [37] and the motion compensation method [29,30] to eliminate decoding artifacts.

## 5. Conclusion

In this paper, a spatio-temporal encoding method using two pairs of orthogonal Golay codes is presented to increase the SNR and contrast of DWC imaging without sacrificing the frame rate. Using the orthogonal and complementary properties of designed codes, two simultaneously transmitted DWs can be separated and compressed through two transmit events with Golay coded excitation. This overcomes the drawback of frame rate reduction when Golay coded excitation is used for DWC imaging. The performance of the proposed OGP-coded scheme was verified through simulations and phantom experiments, demonstrating the feasibility of the proposed method in achieving higher image quality in terms of SNR and contrast. The moving phantom simulations demonstrated that the OGP-coded scheme outperforms the non-coded scheme, although it may suffer from the motion degradation when a large number of DWs was used. Preliminary *in vivo* study proved that the OGP-coded scheme obtains higher image intensity in the human left ventricle compared with the non-coded scheme. The proposed OGP-coded DWC sequence may be beneficial for high frame rate and high quality cardiac imaging.

## Acknowledgements

This study was supported in part by the National Key R&D Program of China (2016YFC0102200 and 2016YFC0104700) and the National Natural Science Foundation of China (NSFC) (81471665 and 81561168023).

## References

- [1] C. Papadacci, M. Pernot, M. Couade, M. Fink, M. Tanter, High-contrast ultrafast imaging of the heart, *IEEE Trans. Ultrason. Ferroelectr. Freq. Control* 61 (2013) 288–301.
- [2] M. Cikes, L. Tong, G.R. Sutherland, J. D'hooge, Ultrafast cardiac ultrasound imaging: technical principles, applications, and clinical benefits, *JACC: Cardiovasc. Imaging* 7 (2014) 812–823.
- [3] J. Grondin, V. Sayseng, E.E. Konofagou, Cardiac strain imaging with coherent compounding of diverging waves, *IEEE Trans. Ultrason. Ferroelectr. Freq. Control* 64 (2017) 1212–1222.
- [4] J. Grondin, M. Waase, A. Gambhir, E. Bunting, V. Sayseng, E.E. Konofagou, Evaluation of coronary artery disease using myocardial elastography with diverging wave imaging: validation against myocardial perfusion imaging and coronary angiography, *Ultrasound Med. Biol.* 43 (2017) 893–902.
- [5] J. Provost, V.T. Nguyen, D. Legrand, S. Okrasinski, A. Costet, A. Gambhir, et al., Electromechanical wave imaging for arrhythmias, *Phys. Med. Biol.* 56 (2011) L1–L11.
- [6] P. Song, H. Zhao, M. Urban, A. Manduca, S.V. Pislaru, R.R. Kinnick, et al., Improved shear wave motion detection using pulse-inversion harmonic imaging with a phased array transducer, *IEEE Trans. Med. Imaging* 32 (2013) 2299–2310.
- [7] M. Couade, C. Flanagan, W.-N. Lee, E. Messas, M. Fink, M. Pernot et al., Evaluation of local arterial stiffness using ultrafast imaging: a comparative study using local arterial pulse wave velocity estimation and shear wave imaging, in: *Proc. IEEE Ultrason. Symp. (IUS)*, 2010, pp. 475–478.
- [8] M. Correia, J. Provost, S. Chatelin, O. Villemain, M. Tanter, M. Pernot, Ultrafast harmonic coherent compound (UHCC) imaging for high frame rate echocardiography and shear-wave elastography, *IEEE Trans. Ultrason. Ferroelectr. Freq. Control* 63 (Mar 2016) 420–431.
- [9] M. Tanter, M. Fink, Ultrafast imaging in biomedical ultrasound, *IEEE Trans. Ultrason. Ferroelectr. Freq. Control* 61 (2014) 102–119.
- [10] R.Y. Chiao, L.J. Thomas, S.D. Silverstein, Sparse array imaging with spatially-encoded transmits, in: *Proc. IEEE Ultrason. Symp. (IUS)*, 1997, pp. 1679–1682.
- [11] T. Misaridis, J.A. Jensen, Use of modulated excitation signals in medical ultrasound. Part III: high frame rate imaging, *IEEE Trans. Ultrason. Ferroelectr. Freq. Control* 52 (2005) 208–219.
- [12] P. Gong, P. Song, S. Chen, Ultrafast synthetic transmit aperture imaging (USTA) using hadamard-encoded virtual sources with overlapping sub-apertures, *IEEE Trans. Med. Imaging* 36 (2017) 1372–1381.
- [13] E. Tiran, T. Deffieux, M. Correia, D. Maresca, B.F. Osmanski, L.A. Sieu, et al., Multiplexed wave imaging increases signal-to-noise ratio in ultrafast ultrasound imaging, *Phys. Med. Biol.* 60 (2015) 8549–8566.
- [14] R.Y. Chiao, X. Hao, Coded excitation for diagnostic ultrasound: a system developer's perspective, in: *Proc. IEEE Ultrason. Symp. (IUS)*, 2003, pp. 437–448.
- [15] T. Misaridis, J.A. Jensen, Use of modulated excitation signals in medical ultrasound. Part I: Basic concepts and expected benefits, *IEEE Trans. Ultrason. Ferroelectr. Freq. Control* 52 (2005) 177–191.
- [16] T. Misaridis, J.A. Jensen, Use of modulated excitation signals in medical ultrasound. Part II: design and performance for medical imaging applications, *IEEE Trans. Ultrason. Ferroelectr. Freq. Control* 52 (2005) 192–207.
- [17] T.X. Misaridis, K. Gammelmark, C.H. Jørgensen, N. Lindberg, A.H. Thomsen, M.H. Pedersen, et al., Potential of coded excitation in medical ultrasound imaging, *Ultrasonics* 38 (2000) 183–189.
- [18] M. O'Donnell, Coded excitation system for improving the penetration of real-time phased-array imaging systems, *IEEE Trans. Ultrason. Ferroelectr. Freq. Control* 39 (1992) 341–351.
- [19] B. Lashkari, K. Zhang, E. Dovlo, A. Mandelis, Coded excitation waveform engineering for high frame rate synthetic aperture ultrasound imaging, *Ultrasonics* 77 (May 2017) 121–132.
- [20] B. Lashkari, K. Zhang, A. Mandelis, High-frame-rate synthetic aperture ultrasound imaging using mismatched coded excitation waveform engineering: a feasibility study, *IEEE Trans. Ultrason. Ferroelectr. Freq. Control* 63 (Jun 2016) 828–841.
- [21] I. Trots, Y. Tasinkevych, A. Nowicki, M. Lewandowski, Golay coded sequences in synthetic aperture imaging systems, *Arch. Acoust.* 36 (2011) 913–926.
- [22] R.Y. Chiao, L.J. Thomas, Synthetic transmit aperture imaging using orthogonal Golay coded excitation, in: *Proc. IEEE Ultrason. Symp. (IUS)*, 2000, pp. 1677–1680.
- [23] F. Zhao, L. Tong, Q. He, J. Luo, Coded excitation for diverging wave cardiac imaging: a feasibility study, *Phys. Med. Biol.* 62 (2017) 1565–1584.
- [24] R.Y. Chiao, L.J. Thomas III, Method and apparatus for ultrasonic synthetic transmit aperture imaging using orthogonal complementary codes, U.S. Patent No. 6,048, 315, 11 Apr, 2000.
- [25] J.A. Jensen, N.B. Svendsen, Calculation of pressure fields from arbitrarily shaped, apodized, and excited ultrasound transducers, *IEEE Trans. Ultrason. Ferroelectr. Freq. Control* 39 (1992) 262–267.
- [26] J.A. Jensen, Field: a program for simulating ultrasound systems, *Med. Biol. Eng. Comput.* 34 (part 1) (1996) 351–353.
- [27] L. Tong, A. Ramalli, R. Jasaityte, P. Tortoli, J. D'hooge, Multi-transmit beam forming for fast cardiac imaging—experimental validation and in vivo application, *IEEE Trans. Med. Imaging* 33 (2014) 1205–1219.
- [28] P. Tortoli, L. Bassi, E. Boni, A. Dallai, F. Guidi, S. Ricci, ULA-OP: an advanced open platform for ultrasound research, *IEEE Trans. Ultrason. Ferroelectr. Freq. Control* 56 (Oct 2009) 2207–2216.
- [29] J. Poree, D. Posada, A. Hodzic, F. Tournoux, G. Cloutier, D. Garcia, High-frame-rate echocardiography using coherent compounding with doppler-based motion-compensation, *IEEE Trans. Med. Imaging* 35 (Jul 2016) 1647–1657.
- [30] K. Kim, J. Hwang, J. Jeong, T. Song, An efficient motion estimation and compensation method for ultrasound synthetic aperture imaging, *Ultrason. imag.* 24 (2002) 81–99.
- [31] J. Wang, J.-Y. Lu, Motion artifacts of extended high frame rate imaging, *IEEE Trans. Ultrason. Ferroelectr. Freq. Control* 54 (2007) 1303–1315.
- [32] C.-C. Tseng, C. Liu, Complementary sets of sequences, *IEEE Trans. Inform. Theory* 18 (1972) 644–652.
- [33] A. Nowicki, I. Trots, P.A. Lewin, W. Secomski, R. Tymkiewicz, Influence of the ultrasound transducer bandwidth on selection of the complementary Golay bit code length, *Ultrasonics* 47 (Dec 2007) 64–73.
- [34] A. Brenner, K. Eck, W. Wilhelm, T. Noll, Improved resolution and dynamic range in medical ultrasonic imaging using depth-dependent mismatched filtering, in: *Proc. IEEE Ultrason. Symp. (IUS)*, 1997, pp. 1475–1480.
- [35] J. Kang, Y. Kim, W. Lee, Y. Yoo, A new dynamic complex baseband pulse compression method for chirp-coded excitation in medical ultrasound imaging, *IEEE Trans. Ultrason. Ferroelectr. Freq. Control* 64 (Nov 2017) 1698–1710.
- [36] P.-C. Li, E. Ebbini, M. O'Donnell, A new filter design technique for coded excitation systems, *IEEE Trans. Ultrason. Ferroelectr. Freq. Control* 39 (1992) 693–699.
- [37] R.Y. Chiao, Method and apparatus for flow imaging using Golay codes, U.S. Patent No. 6,312,384, 6 Nov, 2001.